*Chapter 3.*

*Glider-ADCP toolbox: a MATLAB toolbox for*

*processing active acoustic data onto underwater glider*

# Chapter 3. Glider-ADCP toolbox: a MATLAB toolbox for processing active acoustic data onto underwater glider

## Table of Contents

# Table of figures

## 3.1.    Introduction

Autonomous underwater gliders (Davis et al., 2002) are becoming increasingly important for the collection of oceanographic measurements in observing programs, thanks to their capacity to operate autonomously in all weather conditions, for missions up to several months, and with higher sampling resolution than generally obtained with traditional platforms (Liblik et al., 2016; Rudnick, 2016; Testor et al., 2019)**.** Glider vehicles can autonomously dive to typically up to 1000 m water depth and return to the surface navigating along predetermined sampling paths. It's a low power long duration AUV (up to approximately a year depending on sampling mode and sensors used), which is driven along a saw-tooth path primarily through small changes in buoyancy by altering the volume of the hull (air or oil). Pitch and steerage are enabled by adding wings and altering the center of mass by shifting the battery on the horizontal plane inside the hull (Rudnick et al., 2004). Gliders can carry a range of interchangeable sensor packages, and their low power consumption provides an incredibly detailed look at the water column (high-resolution measurements). As a result, they have been deployed in a wide range of environments: from continental boundary currents to the polar seas, to study aspects ranging from long-term climate variability to fine-scale submesoscale processes (Testor et al., 2019, for a full list of studies and their references). However, these technology platforms have not yet reached the same level of maturity as more traditional oceanographic monitoring platforms (Troupin et al., 2015). This implies that a newcomer to glider data analysis is exposed to many issues and time-consuming tasks that are not common when processing data from more traditional platforms.

Several initiatives as EGO (Everyone's Gliding Observatories, www.ego-network.org), GROOM (Gliders for Research, Ocean Observation, and Management), JERICO (Towards a Joint European Research Infrastructure network for Coastal Observatories, www.jerico-ri.eu), and OceanGliders (www.oceangliders.org) programs are involved in the sharing best practices,

requirements, and scientific knowledge needed to glider operations, data collection, and processing (Testor et al., 2019). As a result, several open-source user-written glider-specific softwares have become available for processing glider data. Notable open access examples include the Coriolis toolbox (EGO gliders data management team, 2017), UEA toolbox (http://www.byqueste.com/toolbox.html), SOCIB packages (Troupin et al., 2015), and more recently GliderTools developed in Python 3.7 (Gregor et al., 2019). Most of these open-source packages offer automated quality control (QC) for CTD (Conductivity, Temperature, Depth) sensors and glider navigation data. GliderTools expands these advances with modules for bio-optical data QC, vertical gridding, and two-dimensional interpolation. These developments cover the main stages of the data management process, including metadata aggregation, data download, advanced data processing, and the generation of data products and figures for the traditional sensors mounted on gliders. However, recent technological advances allowed the integration of more complex sensors onto underwater gliders such as Acoustic Doppler Current Profilers (ADCP) to measure currents (Gentil et al., 2020; Merckelbach et al., 2019; Todd et al., 2017), microstructure to measure turbulence (Merckelbach et al., 2019; Palmer et al., 2015; Wolk et al., 2009), or even Laser In Situ Scattering and Transmissometry (LISST) particle analyzer to characterize suspended particles populations (Miles et al., 2021, 2018) in the water column. A need exists to operate and manage the data streams in real-time and delayed mode, from these new complex sensors.

In the absence of an available processing chain, I had to develop at the beginning of my thesis work a toolbox to process ADCP glider data, to be able to analyze and interpret the current and acoustic backscatter data for hydro-sedimentary issues. In this study, a focus is carried out on the active acoustic glider sensor (ADCP) to derive absolute velocities and their baroclinic component (hydrodynamic), as well as backscatter index (proxy of particulates matter concentration) in the water column. This chapter, combined with a clear annotation of the code,

provides a framework to process acoustic glider data. The toolbox overview and glider setup are described in sections 3.2 and 3.3, respectively. Finally, section 3.4 presents the data chain processing step by step.

## 3.2.      Toolbox overview

The toolbox is available from (https://github.com/mgentil17/mgentil17), without any registration or login required. A dataset is also provided to run the toolbox.

The glider-ADCP toolbox is composed of a set of MATLAB (MATLAB, 2018) scripts and functions designed to process the data collected by a Teledyne Webb Research Slocum glider from recent data-processing methods. Currently, the toolbox version supports the Slocum G1 model. This toolbox is designed to provide a delayed mode quality control on the physical, bio-optical, and acoustic sensor on the glider's suite. Delayed mode data includes all data collected from ocean gliders that are stored on the vehicle during its mission and need to be checked thoroughly by PI and against other measurements (ship-based observations, satellites). The toolbox operates on data conversion, advanced data processing, and the generation of data products and figures.

Figure 3.1 presents the workflow of the glider-ADCP toolbox, which is divided into 8 steps. The toolbox is organized around two main scripts (rectangles with red outlines). The former, *Glider_Adcp_main_program.m*, is summarized by the processing chain (step 0 to 7) and calls all the functions used in the toolbox. For each processing step, the external and internal data (circular boxes), the functions in the modules (grey rectangles) and their dependencies (arrows), as well as the outputs (figures and files) are made explicit. The toolbox is built to output 5 levels (L0 to L4) of MATLAB files (. mat), related to different levels of processing steps described in Figure 3.1 and
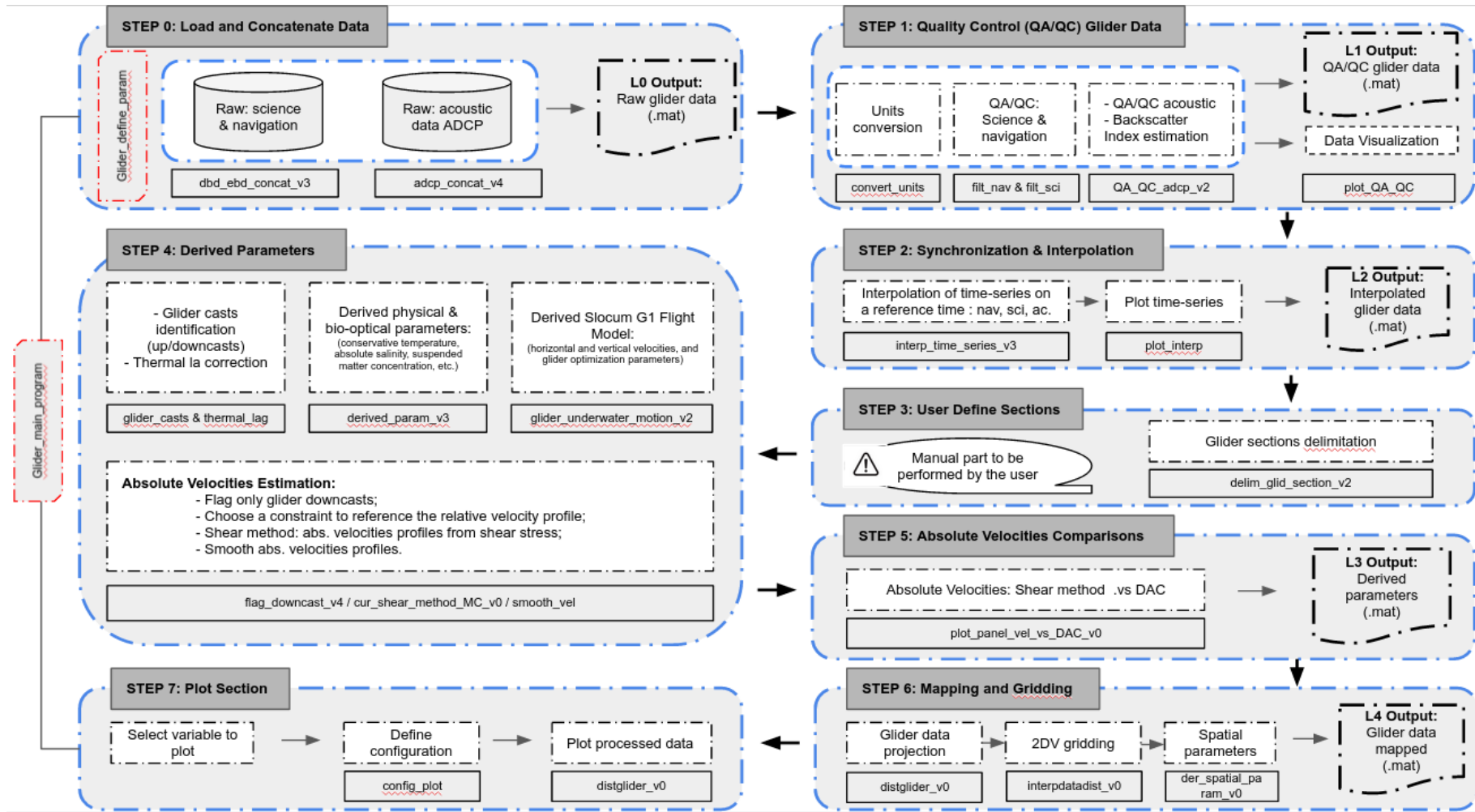
**Figure 3.1**: Scheme of the Glider-ADCP treatment chain step by step (initial step "0" to the final one "step 7"). The white rectangles show the processing action performed in each of the modules. The grey rectangles represent the codes (. m) associated with the action boxes. Black and grey arrows show dependencies between the different modules and the different action boxes, respectively. Five levels of outputs (L0 to L4) are produced from the processing chain. Finally, the rectangles with red outlines are the two main scripts of the toolbox.

detailed    and    applied    in    section 3.4    (i.e.,    Processing    Steps).    The    latter    script,
*Glider_ADCP_define_param.m*, is the script that declares the parameters chosen by the user for
each processing step and that is loaded in the *Glider_Adcp_main_program.m* in the initial step
(step 0). The parameterization stage is essential to ensure the correct processing of data in steps 1 to
6 and is also described in section 3.4.

## 3.3.    The Glider-ADCP

### 3.3.1. Explorer ADCP setup

An Explorer Doppler Velocity Log with Acoustic Doppler Current Profiling capacity
(Explorer ADCP) was integrated into a special payload bay on the Slocum glider (Fig. 3.2a). The
Explorer ADCP has a downward facing transducer which was tilted forward by 11°, enabling to
compensate for the pitch of the glider during downcasts. The inclination of the transducer optimized
the three-beam measurements on the 26° pitched glider downcasts with the three forward ADCP
beams oriented 15° from vertical, and with the fourth, 45° aft relative to the glider (Fig. 3.2b). The
offset of 11° represents the best compromise between optimizing for beam position and minimizing
the hydrodynamics drag penalties of the mounting (Mullison et al., 2013). However, this fixed
forward configuration rendered the device unsuitable for collecting measurements during ascent.
Indeed, the non-rotated orientation of the head does not allow respecting the assumption about
symmetry (beam pairs), during upcast measurements as shown in Fig. 3.2b (Mullison et al., 2013).
For this reason, only downcast measurements were used in this study (black line in Fig. 3.2c).

### 3.3.2. Glider operation

In this study, we deployed a Slocum glider equipped with a CTD, an optical payload, and a
downward looking ADCP (Fig. 3.2a). The Teledyne Webb Research Slocum glider (G1) can
autonomously dive to typically up to 200 m water depth. The adjustment of its buoyancy allows it

to navigate along a saw-tooth path through the water column (Fig. 3.2c). Continuously CTD and optical measurements are acquired by the glider along its ascent and descent, according to the sampling frequency user-defined. Also, ADCP periodically records: (i) echo intensity measurements to estimate backscatter index, which is a proxy of SPM concentration, (ii) the relative velocities measurements to estimate absolute velocities, and (iii) the bottom track measurements, which is the direct measure of speed over the ground when in range of the bottom. In this study, we used an Explorer ADCP of 614 kHz, which allows measuring echo intensity and relative velocity in the water column, only during downcast (see section 3.1), to a maximum range of 40–50 m (gridding area in Fig. 3.2c). From this device frequency, the first bottom track measurements are detectable around 50 meters until 2 m above the seabed (green line in Fig. 3.2c), which corresponds to the inflection point of the glider. During surfacing, the glider uses GPS positioning to estimate the difference between the expected surface location from underwater dead reckoning and the GPS fixes. Such position difference, dependent on the duration of the dive, allowed to estimate the depth-averaged current (DAC) between two surfacings (Fig. 3.2d) (Eriksen et al., 2001; Rudnick et al., 2018). Also during surfacing, the glider records GPS fixes, to transfer data to land and to receive any new information about its route configuration. This operation takes between 10–15 min, where the glider is subject to wind and currents forcing, resulting in surface drift (red line in Fig. 3.2c). In coastal environments, multiple yos (upcast/downcast pairs) are the standards (Fig. 3.2d) to limit the glider's surfacing to reduce the risk of collision with ships or topography (coast). During a sequence of multiple yos, the glider dive to typically 2 m above the bottom and ascent to 1 m from the surface (dashed line blue in Fig. 3.2c), leading to an under-sampling of the surface layer (0–1 m).
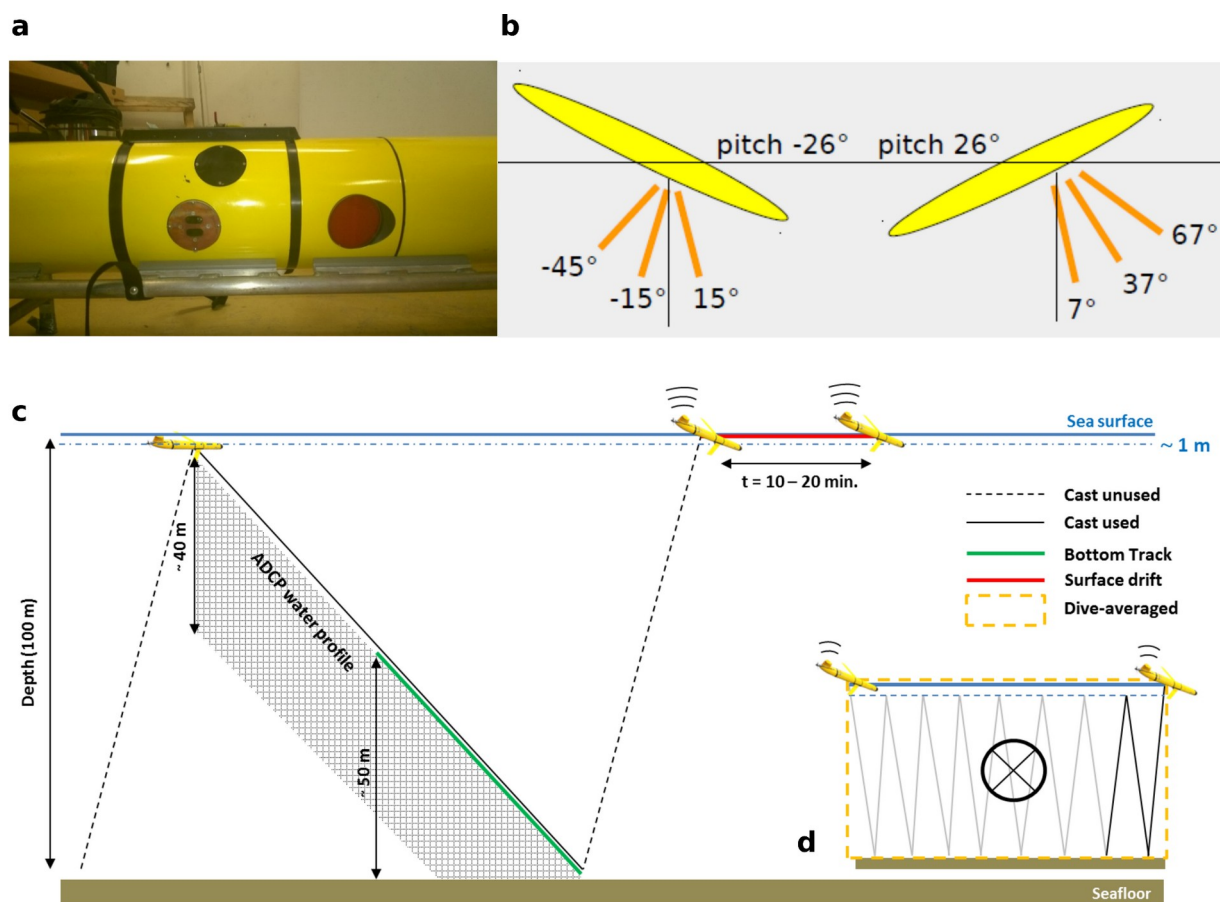
**Figure 3.2**: (a) A view of the BBFLCD optical payload (black) and Explorer ADCP payload (red) integrated into a G1 Slocum glider (photo credit: Gaël Many). (b) Flight orientations showing relative beam angles from a downward looking Explorer ADCP. (c, and d) Glider operation and data acquisition.

### 3.3.3. Glider deployments

Three deployments of a Slocum glider equipped with an active acoustic sensor were carried out in 2016, 2017, and 2018 over the micro-tidal continental shelf of the Gulf of Lions in the NW Mediterranean (Fig. 3.3a), as part of programs to study sediment flux dynamics during extreme events (flood and storm). A total of 3 months of acquisition, 31 sections, and more than 12,700 profiles were recorded for these deployments and were used to develop the toolbox. In this study, the dataset provided to run the glider-ADCP toolbox corresponds to the deployment carried out in winter 2017 (Fig. 3.3b). Examples of profiles of the experiments are used to illustrate the toolbox capacities in section 3.4.
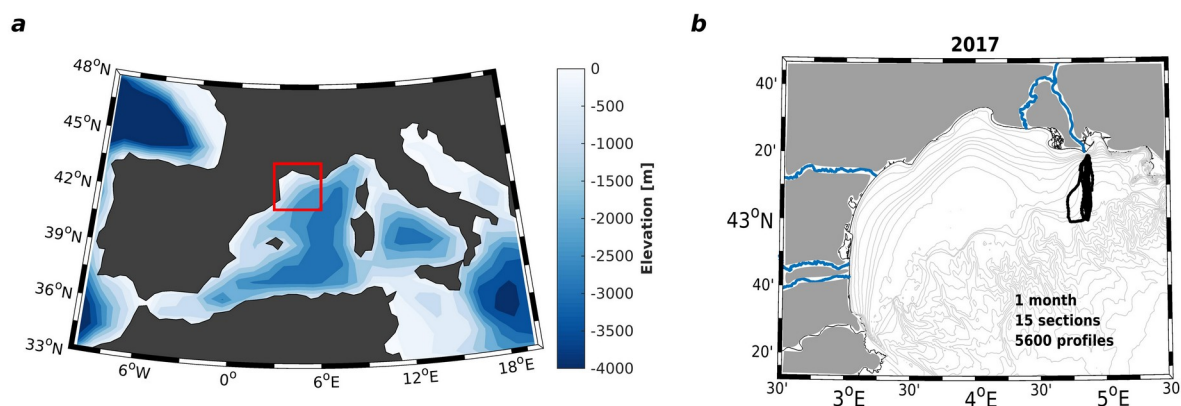
**Figure 3.3**: (a) Western Mediterranean, the Gulf of Lions is located by a red square. (b) Glider-ADCP deployment (black lines) over the Gulf of Lions shelf in winter 2017.

## 3.4.    Processing steps

### 3.4.1.  User-defined parameters

*Glider_ADCP_define_param.m* is one of the two main scripts of the toolbox. In this script, we have defined the set of variables involved in data processing and on which the user can adjust the values according to the scientific processes studied. The main parameters to be filled in are:

- Conversion and calibration of sensors values;

- The magnetic declination for glider compass;

- The configuration of ADCP (pitch inclination, conversion factor) and threshold values for control quality data (correlation signal, velocity intensity, time lag, bottom track offset);

- The reference time to synchronize and interpolate data;

- Glider parameters that will be optimized in the flight model (glider volume, mass, hull compressibility, and parasite drag);

- Options for the parameters optimization;

- Parameters to process acoustic data (bin size, standard deviation of a single ping measurement, number of iterations for Monte-Carlo simulations, vertical and horizontal filters);

- Reference positions and projection angle for mapping the data;

- Vertical and horizontal resolution for gridding processed data.

## 3.4.2. Step 1: quality control of glider data – output level 1 files

The different sensors are processed separately because the temporal data are not synchronized and may have different sampling resolutions. In this study case, the navigation and science bay has a sampling frequency of 4 s and acoustic data of 10 s. During this step, first simple unit conversions and factory calibrations are applied to the science, navigation, and acoustic bay. In a second stage, several filters are applied:

*Science and navigation data*—the compass data are corrected for magnetic declination, gaps of pressure are removed, as well as glider position outliers, and null values. Figure 3.4 shows that ~8% of the navigation, ~55% of CTD, and ~51% of bio-optical data are removed after applying these filters. The majority of the removed data are empty cells because the time vector increments every 2 s. Even though science and navigation have the same sampling rate (4 s), dead reckoning estimates the position of the glider at each time increment, explaining the small amount of data removed for navigation.

*Acoustic data*—raw ADCP data were subjected to a quality checking algorithm to mask low-quality data as well as to correct data. Following Todd et al. (2017), a pipeline of operations was set up: to correct the speed of sound using an average salinity value of 38; to correct time lag; to correct the real depth of each bin from roll and pitch effects; to mask instrumental data according to the factory threshold of 64 counts of the correlation signal (Gordon, 1996); to mask relative water
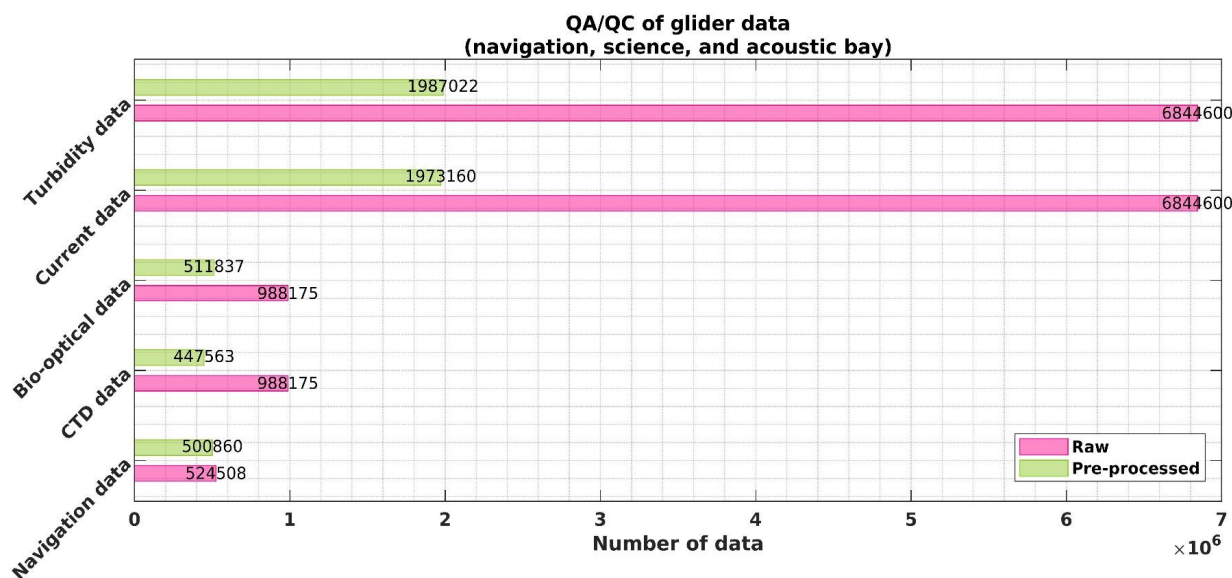
**Figure 3.4**: Control quality (QA/QC) carried out on glider data: for navigation, science (science and bio-optical), and acoustic bay (current and turbidity). Raw and pre-processed data after applying the thresholds defined in the Glider_ADCP_define_param.m are in pink and green, respectively.

velocities and bottom-track velocities that exceed 0.75 m s$^{-1}$. Figure 3.4 shows that ~70% of currents and turbidity data are removed. The acoustic data are very noisy, and applying only the factory threshold reduces the data range by 50 to 60%. At the end of these operations, the L1 matrix file containing pre-processed glider data is generated.

### 3.4.3. Step 2: synchronization & interpolation – output level 2 files

During this step, the user defines the temporal limits of the study, as well as the time step between two measurements. The data from each sensor are synchronized and interpolated to this new reference time. The user should be careful to choose a time step in accordance with the sampling rate of the sensors. In our study case, we chose to synchronize CTD, bio-optical, and navigation data with ADCP data, which have the lowest resolution acquisition, and interpolate to the same periodicity (10 s). Figure 3.5 shows an example of the interpolation of navigation (pitch, roll, heading), CTD (temperature), and bio-optical (backscatter and chlorophyll-a) data. At the end
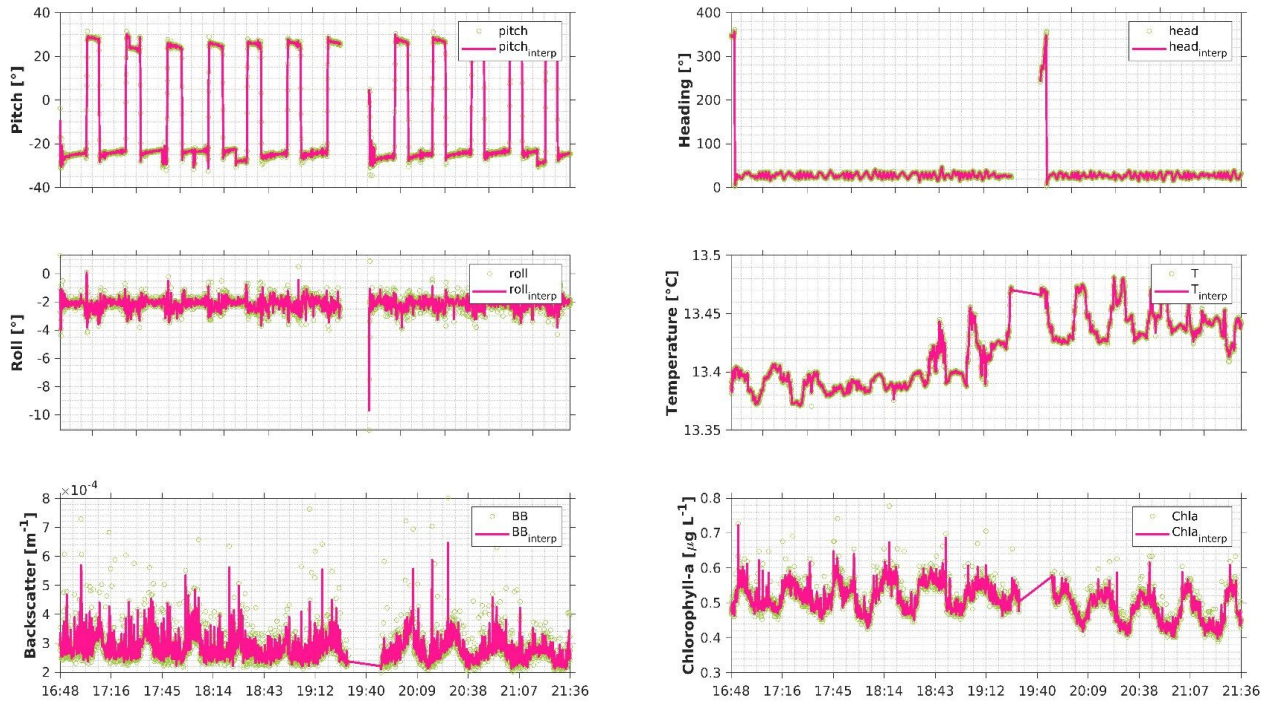
**Figure 3.5**: Interpolation of glider time series: raw data and interpolated data are in green and pink, respectively.

of these operations, the L2 matrix file containing synchronized and interpolated glider time series is generated.

### 3.4.4. Step 3: user-defined sections

During this step, the user defines manually one or more sections over the deployment, called section(s) of interest(s) (SOI[s]). Data processing will be performed on the SOI(s). It is necessary to choose a positioning variable (longitude or latitude) to be plotted as a function of time. Then a dialog box is displayed, where the user defines the number of sections to process (Fig. 3.6). Finally, each section chosen needs to be delimited by two clicks on the plot, (start and endpoints). Figure 3.6 shows an example where latitude is chosen to delimit a SOI.
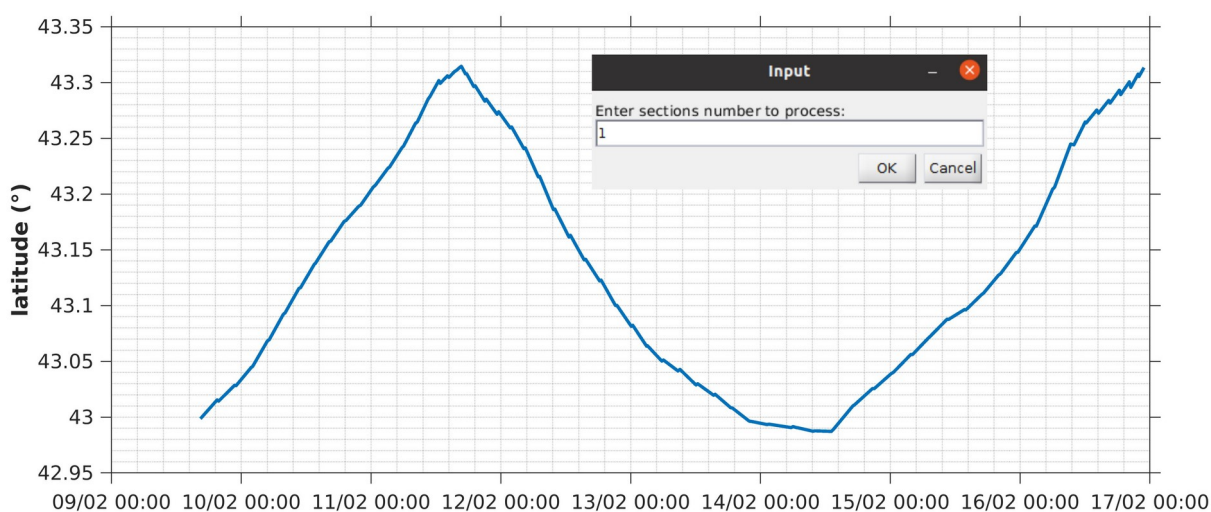
**Figure 3.6**: Latitude as a function of time to delimit section of interest (SOI). The user needs to select the number of sections to keep for data processing.

## 3.4.5.  Step 4: derived parameters – data processing

The objective of this step is to output well-referenced trajectory data with derived measurements and corrections over the SOI. To generate the derived measurements and corrections, operations are applied in the following order:

### *3.4.5.1.     Glider profiles and thermal lag corrections*

First, the pressure of the different sensors (CTD, ADCP, and glider navigation) are compared and adjusted to obtain a reference pressure vector. A gradient threshold on the reference pressure is used to identify dive and ascent glider profiles. At this stage, the thermal-lag correction on CTD data is applied, following the work of Garau et al. (2011). This operation is very time-consuming. The user needs to select several combined profiles (dive/ascent) for which the correction is calculated. Then the average correction is applied to the whole time series. Figure 3.7 shows the result of the average thermal lag correction on a temperature and conductivity profile, after a calculation made on 50 combined profiles of ascents and dives.
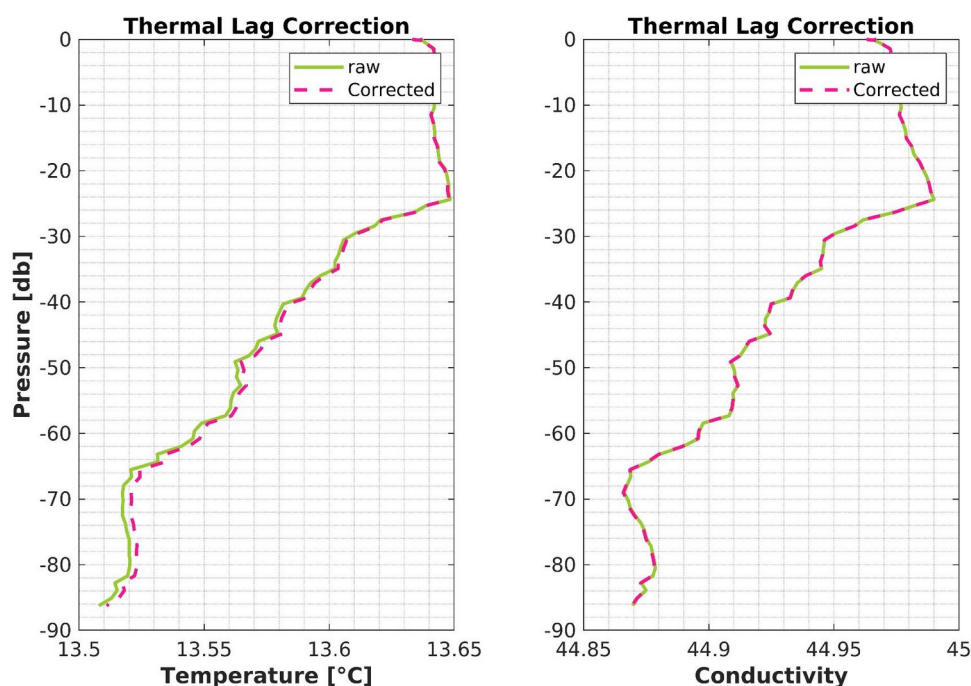
**Figure 3.7**: A profile of temperature and conductivity with raw data (green) and corrected from thermal lag (pink), following the work of Garau et al. (2011).

### 3.4.5.2. *Physical and bio-optical parammeters*

Once the thermal lag is corrected a series of physical parameters can be derived. Salinity, potential temperature, depth, density, Brunt-Väisälä frequency, and others were derived using the TEOS-10 equation (McDougall and Barker, 2011). Furthermore, this toolbox was designed to study hydro-sedimentary processes. The user can load the calibration file of the optical sensor used during the glider deployment, and the suspended particulates matter concentration is derived from the calibration coefficients.

### 3.4.5.3. *Glider flight model*

At this stage, a series of operations is applied to estimate vertical and horizontal glider velocities relative to the water in each point of its path, based on a glider quasi-static flight model developed by Merckelbach et al. (2010). A schematic view of the forces exerted on the glider is represented in Figure 3.8.
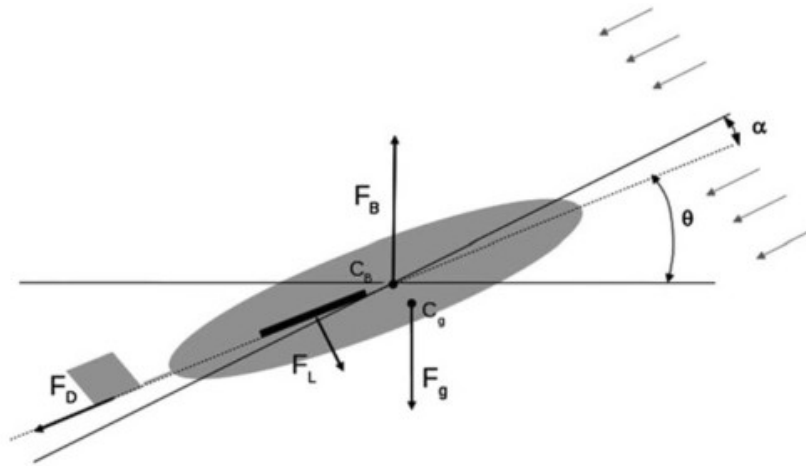
**Figure 3.8**: Schematic view of a glider flight on a vertical plane: buoyancy force $F_b$, gravity $F_g$, lift $F_L$, and drag $F_d$; the sum of attack angle $\alpha$ and pitch $\theta$ makes the glide angle $\gamma$ from Margirier et al. (2017).

The glider is modeled in a steady-state flight and in the absence of vertical movement. The projections of the glider-static equilibrium on the vertical and horizontal thus give:

$$(z): F_B - \cos(\gamma) F_L - \sin(\gamma) F_d - F_g = 0 \tag{3.1}$$

$$(x): \cos(\gamma) F_d - \sin(\gamma) F_L = 0 \tag{3.2}$$

with $F_b$, $F_g$, $F_L$, $F_d$, respectively the buoyancy, gravity, lift and drag force. Typical values of the different parameters are given in Table 1 of Margirier et al. (2017).

$$F_b = g\rho\left(V_g\left(1 - \epsilon P + \alpha_T(T - T_0)\right) + \Delta V_g\right) \tag{3.3}$$

$$F_g = m_g g \tag{3.4}$$

$$F_L = \frac{1}{2}\rho S U^2 a\alpha \tag{3.5}$$

$$F_d = \frac{1}{2}\rho S U^2 \left(C_{D_0} + C_{D_1}\alpha^2\right) \tag{3.6}$$

The vertical water velocity is estimated as the difference between the velocity derived from the rate of change of pressure and that predicted by the glider flight model. Vertical movements of the water are minimized (the model makes the hypothesis there are none) over a 24h period (long

enough to consider that the mean vertical velocities are null) (Margirier et al., 2017). The term on the left in equation 3.7 is therefore equal to zero.

$$w_{water} = \frac{dz_p}{dt} - w_{glider}$$
(3.7)

The steady-state flight model requires four calibration parameters, the parasite drag coefficient $(C_{D_0})$, glider volume (at atmospheric pressure) $(V_g)$, hull compressibility $(\epsilon)$ and the glider mass $(m_g)$, which are found by minimizing a cost function based on the variance of calculated vertical water velocity.

$$J(C_{D0}, \epsilon, V_g, m_g) = \sum (\frac{dz_p}{dt} - w_{glider})^2$$
(3.8)

The optimized parameters are used to derive the angle of attack $(\alpha)$ and the glider speed along its trajectory $(U)$.

$$\alpha = \frac{C_{D_0} + C_{D_1}\alpha^2}{a \tan(\theta + \alpha)}$$
(3.9)

$$U = \frac{2(F_b - F_g)\sin(\gamma)}{\rho S[C_{D_0} + (C_{D_{1_w}} + C_{D_{1_h}})\alpha^2]}$$
(3.10)

We then obtain the glider's vertical (eq. 3.11) and horizontal (eq. 3.12) velocities. The east-west and north-south components of the glider are derived from the horizontal velocity ($U_{glider}$).

$$W_{glider} = U sin(\gamma)$$
(3.11)

$$U_{glider} = U cos(\gamma)$$
(3.12)

To assess the quality of the flight model, we compared the vertical glider velocity estimated from optimization and the pressure sensor (Fig. 3.9). As expected, the vertical water motion is on average equal to zero (in blue, Fig. 3.9), assuming still water in the flight model. Furthermore, the robustness of the method is highlighted by the fact that the extracted vertical velocities are not affected by the glider vertical movement (dive/ascent). Indeed, when the glider switches from a

**Glider Vertical Velocities**
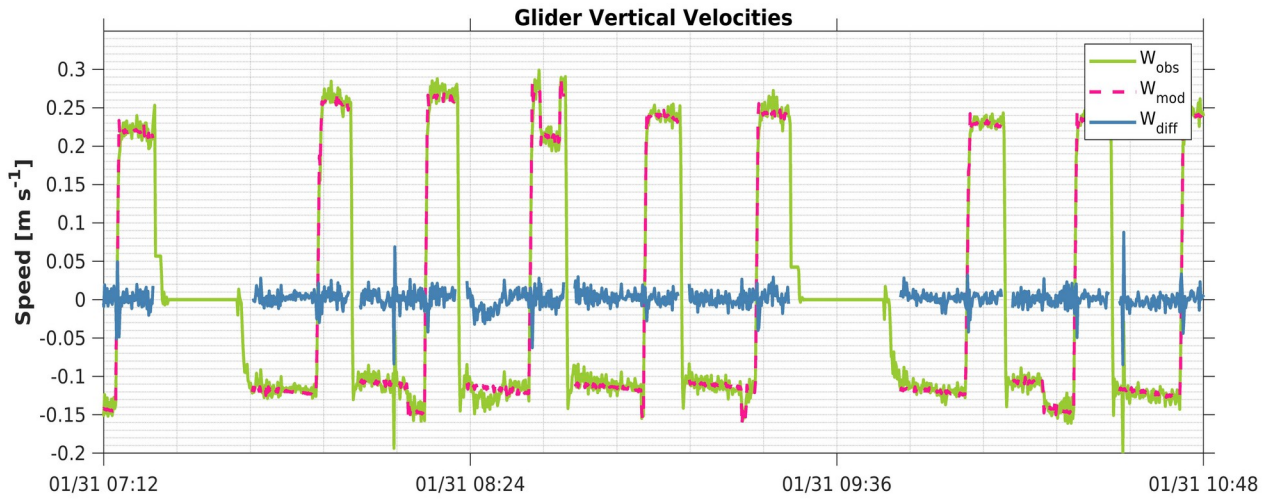


**Figure 3.9**: Flight parameters and resulting water vertical velocity in a steady-state hypothesis. Glider vertical velocity $\left(w_{glider}\right)$ (pink), pressure gradient induced velocity $\left(\dfrac{dz_p}{dt}\right)$ (green), and water vertical velocity $\left(w_{water}\right)$ (blue).

downward to an upward motion, the water vertical velocity remains coherent (variation <5 cm s$^{-1}$). During the second dive, we can see a spike in the data. This is probably because the pitching battery moved, and we use a steady-state model. The steady-state model does not include these changes and adapts instantly, in contrast to the glider. These spikes are filtered in the toolbox.

The validation of the glider flight model allowed us to recalculate the glider's velocity in each component and at each point of its path in the water column. Figure 3.10 shows that with the initial parameters the vertical and horizontal glider's velocities are overestimated, especially during a dive. An average difference of about 3 and 15 cm s$^{-1}$ is found between the initial and optimized velocities for the vertical and horizontal components, respectively. While during upcast, vertical velocities are similar and a difference of 5 cm s$^{-1}$ is found on the horizontal component. The optimized average velocities are therefore of the order of 0.15 and 0.25 m s$^{-1}$ in descent for the vertical and horizontal components, respectively, and of 0.25 and 0.5 m s$^{-1}$ for upcast. The accuracy of the glider motion is fundamental to derive the absolute water velocities.
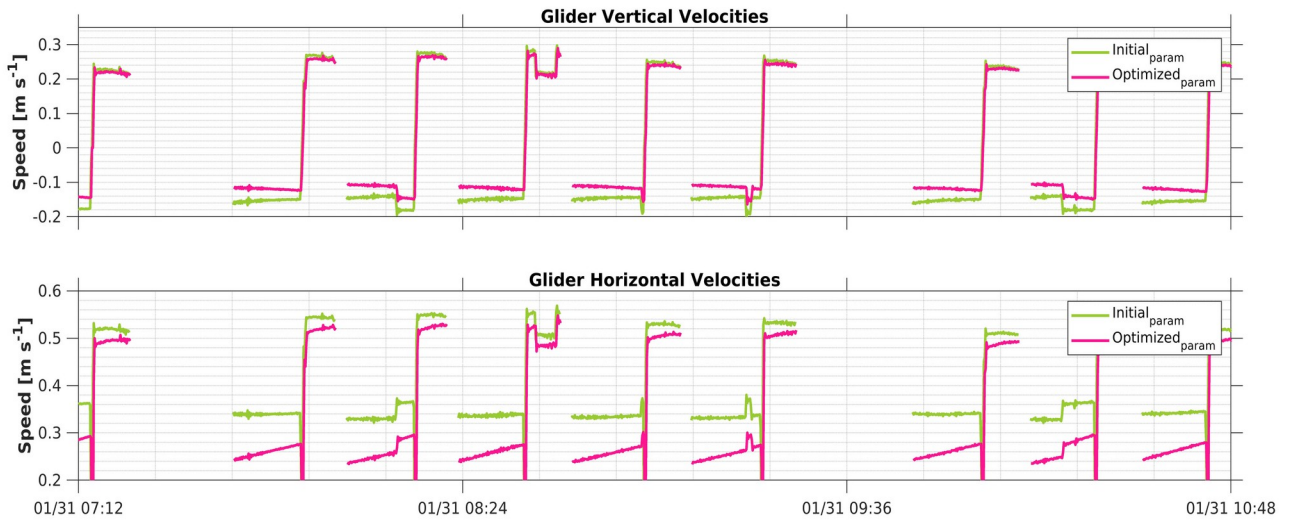
**Figure 3.10**: Glider's velocity components: (top) vertical velocity, and (bottom) horizontal velocity. The glider's velocity from the initial parameters is shown in green, while those from the optimized parameters from the quasi-steady flight model (Merckelbach et al., 2010) are in pink.

### 3.4.5.4. *Absolute velocities and backscatter index*

At this step, the selection of downcasts only is carried out from the glider-ADCP toolbox, due to the ADCP setup (see section 3.3.1).

#### 3.4.5.4.1. Backscatter index estimates

The received level (RL) of the acoustic return along each beam was converted into the backscatter index (BI, in dB) from Mullison, (2017).

$$BI = 10 \, log_{10}\big(10^{(Kc(RL-Er/10))} - 1\big) + TL_w + TL_g \tag{3.13}$$

where Kc is the count to dB factor (0.61 for the ADCP used in this work), RL the received level in counts, Er the noise in counts (50 counts), TLw the loss due to absorption by seawater (Francois and Garrison, 1982), and TLg the loss due to geometrical spreading. The computation of the speed of sound was based on the Explorer temperature sensor and an average salinity value of 38.
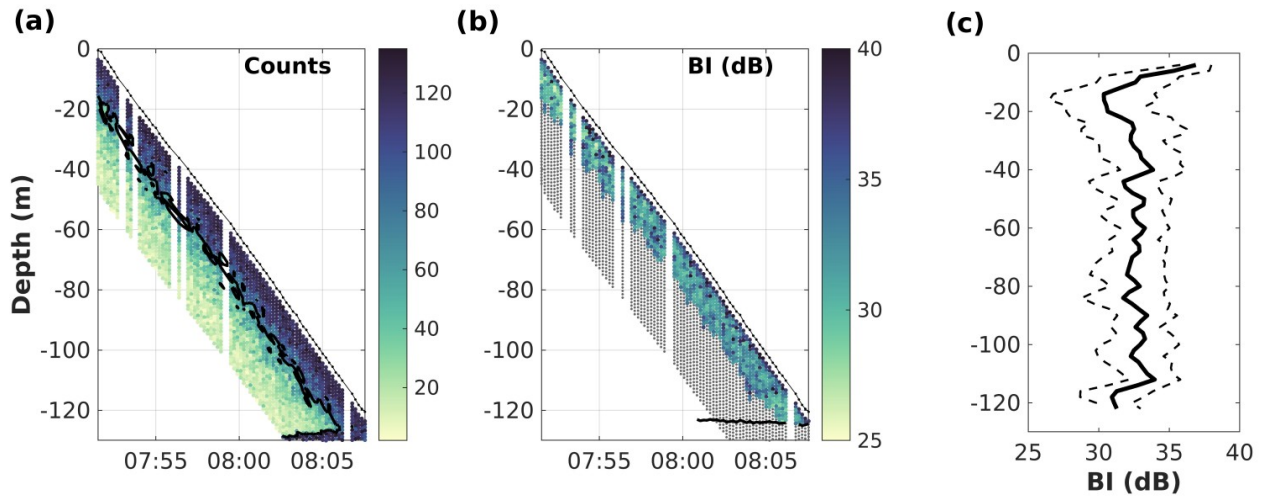
**Figure 3.11**: Example of measurements carried out by the Acoustic Doppler Current Profiler (ADCP) during a descent of the glider. (a) The swath of the count signal for each cell of the multiple water profiles. The threshold of 64 counts used to discard erroneous values is shown in black. (b) Filtered backscatter index (BI) measurements (dB). Discarded values are shown in gray. A black line shows bottom detection. (c) Reconstructed median backscatter index profile and associated standard deviation from Gentil et al. (2020).

ADCP provides a series of overlapping profiles (Fig. 3.11a) over a typical vertical range of O(20) m after the control quality (Fig. 3.11b). The successive profiles of the backscatter index were stacked to reconstruct the profile over the entire water column from the median values of the overlapping data at each level (Visbeck, 2002). The associated uncertainty corresponds to the standard deviation of the stacked values for each bin (in this study case is 1 m depth bin). A final three-point centered moving-average filter was applied to eliminate the high-frequency noise (Fig. 3.11c).

### 3.4.5.4.2. Absolute velocities estimates

As backscatter index profiles, the successive relative velocity profiles were stacked to reconstruct the profile over the entire water column from the median values of the overlapping data at each level (Fig. 3.12a-b). During post-processing, methods are used to remove the glider's motion ($u_{glider}$) from relative velocity measurements of ADCP ($u_{ADCP}$) and to apply absolute velocity

constraints to obtain profiles of absolute horizontal currents ($u_{ocean}$). The ADCP measurement

principle according to the time ($t$) and depth at each bin ($i$) is as follows:

$$u_{ADCP}^{(t,i)} = u_{ocean}^{(t,i)} + u_{glider}^{(t,i)} \tag{3.14}$$

In this study, three methods were used to estimate the absolute velocities: (i) the "shear"

method, (ii) the "direct" method, and (iii) the "inverse" method, described below.

***(i) The "shear" method***—is based on the work of Firing and Gordon, (1990), with the

assumption that glider velocity is constant for each profile and can, therefore, be eliminated. After

reconstructing the shear of the current over the whole water column (Fig. 3.12c), its integration

allows obtaining a relative water velocity profile (Fig. 3.12d). At this step, a constraint is required,
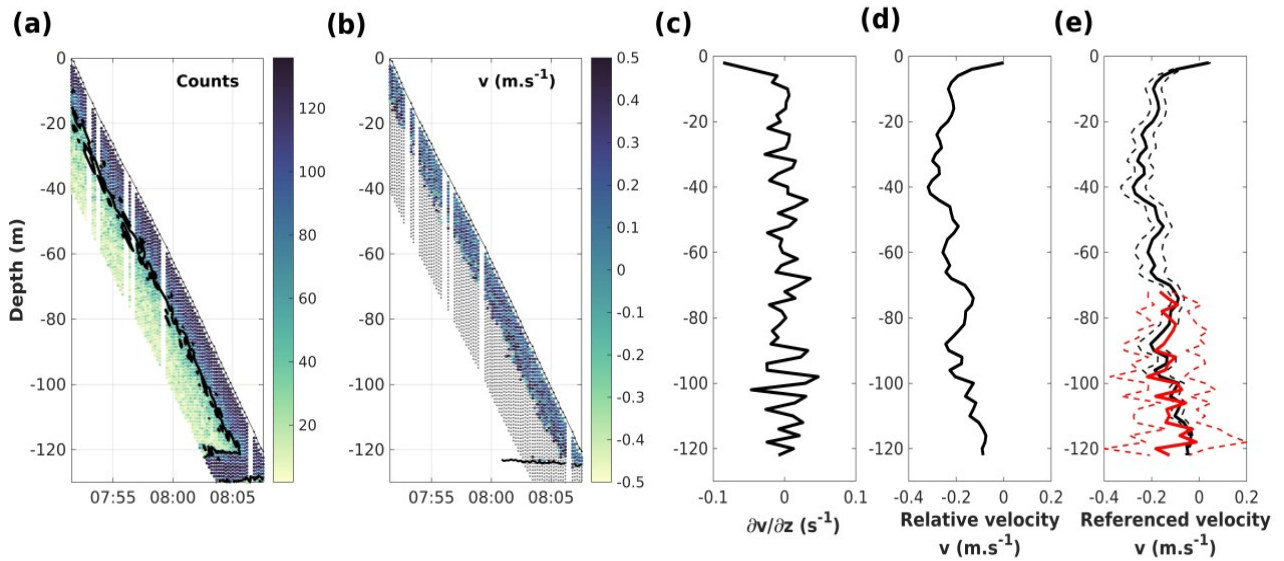


**Figure 3.12**: Example of measurements carried out by the ADCP during a descent of the glider. (a) The swath of the counts signal for each cell of successive water profiles. The empirical threshold of 64 counts used to discard erroneous velocity values is shown in black. (b) Filtered raw northward velocity measurements (m s$^{-1}$). Discarded values are shown in grey. The black line shows bottom detection. (c) Mean profile reconstructed after stacking successive profiles of the vertical derivatives of measured currents. (d) Integrated relative velocity profile. (e) Absolute velocity profile (black line) after adjustment with near-bottom current measurements derived from bottom tracking (red line), dashed lines indicate uncertainties (standard deviation) for each variable from Gentil et al. (2020).

corresponding to a barotropic velocity component, to derive absolute water velocity profiles. Absolute velocity is estimated by adjusting the relative velocity profile to the current velocity measured by the barotropic constraint (Fig. 3.12e). The user chooses the constraint to apply from the toolbox, either the depth-averaged current (DAC), either the bottom track (BT) (Fig. 3.12e). When the glider performs multiple yos (downcast/upcast) between two surfacings, as is often the case in coastal deployments, we recommend using the BT if it meets the quality control (i.e., no offset). Indeed, the BT is specific to each downcast, while the DAC is calculated between two surfacings (i.e., on 6 downcasts in our study case). Furthermore, the lack of ADCP data during upcast and in the surface layer may result in a bias between the average ADCP data and the DAC.

Uncertainties regarding absolute water velocities vary depending on the ADCP settings (mainly cell size, instrument frequency, pulse length, and the number of pings per ensemble) (Gordon, 1996). The user must fill in the error (standard deviation) associated with single ping measurements in the *Glider_define_param* script. To estimate the uncertainty of the relative velocity estimates, we performed a Monte-Carlo simulation based on 500 iterations, with initial velocity values sampled randomly according to a normal distribution centered on the measured value for each bin of each profile during the downcast. Finally, an average standard deviation of the absolute velocity—calculated from the sum of variances of the relative velocities and the constraint selected—is estimated (Fig. 3.12e).

A moving average on vertical (depth) and horizontal (time) windows can be applied on the absolute velocities of the SOI (to be defined in *Glider_define_param.m*) because the "shear method" is relatively noisy.

*(ii) The "direct" method*—is based on the work of Merckelbach et al. (2010), with the estimation of glider motions by a steady-state flight model (see section 3.4.5.3, equations 3.1 to 3.12). The horizontal glider velocity is then subtracted from the ADCP measurements at each depth.

Uncertainties regarding absolute water velocities are calculated from the sum of variances of the relative velocities and glider motion from the steady-state flight model.

**(iii) The "Inverse" method**—considers a system of equations formed by the relationships between the known ADCP velocity measurements ($d$), unknown current and glider speeds ($m$), and known uncertainties or noise ($n$). Constraints can be added to this system such as the measured glider speeds near the bottom from the bottom track, and the glider motions determined from an optimized flight model. Each of these constraints is assigned a weight (Todd et al., 2017; Visbeck, 2002) that can be adjusted by the user. The equation system is written in matrix form (Visbeck, 2002).

$$d = Gm + n \qquad (3.15)$$

where the vector $d$ represents all ADCP velocities from different depths within the water column. $n$ represents the noise due to imperfect measurements $d$ and imperfect prediction of the absolute velocity field by $Gm$. The unknown ocean velocity profile and motion of the glider are combined into a single vector, which are related to the observations $d$ by the model matrix $G$, as shown in the example below. This method is particularly flexible because additional constraints can be added, by simply adding rows to the initial vector $d$ and matrix $G$.

$$
d = \begin{bmatrix} u_{1,1} \\ u_{1,2} \\ u_{1,3} \\ u_{2,1} \\ \vdots \\ u_{3,1} \\ \vdots \\ u_{20,3} \end{bmatrix}, \quad
m = \begin{bmatrix} u_{ctd,1} \\ u_{ctd,2} \\ u_{ctd,3} \\ \vdots \\ u_{ctd,20} \\ - \\ u_{ocean,1} \\ u_{ocean,2} \\ u_{ocean,3} \\ \vdots \\ u_{ocean,10} \end{bmatrix}, \quad
G = \left\{ \begin{array}{ccccc|ccccc} 1 & 0 & 0 & \cdots & 0 & 1 & 0 & 0 & \cdots & 0 \\ 1 & 0 & 0 & \cdots & 0 & 0 & 1 & 0 & \cdots & 0 \\ 1 & 0 & 0 & \cdots & 0 & 0 & 0 & 1 & \cdots & 0 \\ 0 & 1 & 0 & \cdots & 0 & 0 & 1 & 0 & \cdots & 0 \\ \vdots & \vdots & \vdots & \ddots & \vdots & \vdots & \vdots & \vdots & \ddots & \vdots \\ 0 & 0 & 1 & \cdots & 0 & 0 & 0 & 1 & \cdots & 0 \\ \vdots & \vdots & \vdots & \ddots & \vdots & \vdots & \vdots & \vdots & \ddots & \vdots \\ 0 & 0 & 0 & \cdots & 1 & 0 & 1 & 0 & \cdots & 1 \end{array} \right\}.
$$

The solutions of the systems are given by equation 3.16. To solve this system of linear equations, we use the least squares method, minimizing the squared error between $d$ and its estimated value $d^{pre}$. The error prediction, which the least squares method tries to minimize, is given by equation 3.17.

$$m = G^T [G G^T]^{-1} d \qquad\qquad (3.16)$$

$$E = \left[ \sum_{i=1}^{N} |d_i - d_i^{pre}| \right]^2 \qquad\qquad (3.17)$$

The three methods, presented above, should give similar results for the estimation of absolute velocities in the water column. However, despite a good optimization of the glider vertical velocity from the steady-state flight model (Fig. 3.9), the glider horizontal velocity appears particularly weak around 0.25 m s⁻¹ (Fig. 3.10b) compared to the expected velocity of around 0.35-0.4 m s⁻¹. The difference between the calculated and expected glider horizontal velocity is of the same order of magnitude as the difference between the absolute velocities estimated from the "shear" and the "direct" method. In addition, the "direct" method does not allow estimating absolute velocities for the first 10 m. This is the depth by which the glider has traveled several body lengths after its inflection point and for which acceleration terms can be reasonably neglected (Merckelbach et al., 2010). Concerning the "inverse method", it has the advantage of being particularly flexible since multiple constraints can be easily incorporated (Todd et al., 2017). However, glider horizontal velocity derived from the flight model cannot be used as a constraint due to the uncertainties on the magnitude mentioned previously. Therefore, only one constraint is available to reference the relative water velocity profile in our study case, the bottom track. This constraint can only be applied to the lower part of the profile when the seabed is in the range of the ADCP measurements. The lack of additional constraints makes it impossible to reference the relative velocity profile at the upper part of the water column. For all these reasons, we chose to use the "shear" method to

estimate absolute velocities in the water column in this thesis work. The "inverse" and "direct" methods have therefore not been implemented in the toolbox.

### 3.4.6.  Step 5: validation of current measurements – output level 3 files

At this step, the robustness of the absolute velocity estimate is assessed, from an "external" current measurement, the DAC (see section 3.2 for the calculation). To assess the quality of the ADCP measurements compared to this independent estimate of the currents, we contrasted the residual current velocities and direction computed from the downcast ADCP data between two surfacings with the corresponding DAC estimates (Fig. 3.13). The two estimates of the integrated average current over the water column were broadly comparable and reproduced the main inversions and intensifications of the currents.
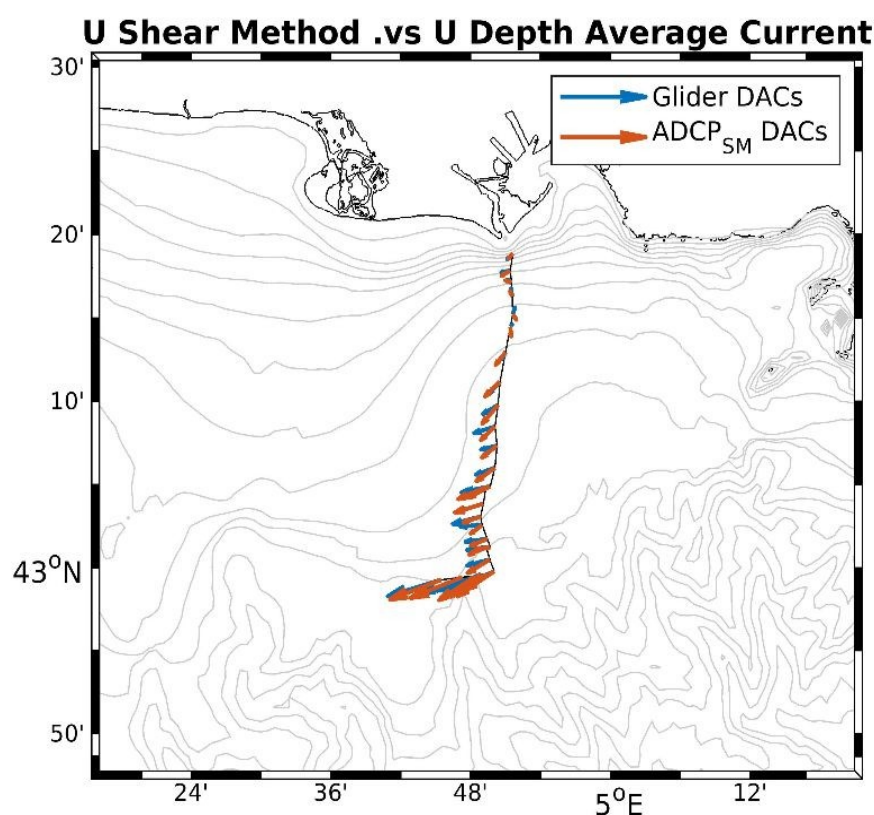


**Figure 3.13**: Comparison of depth-averaged current (DAC) vs. ADCP-derived current from the "shear method", on the section of interest.
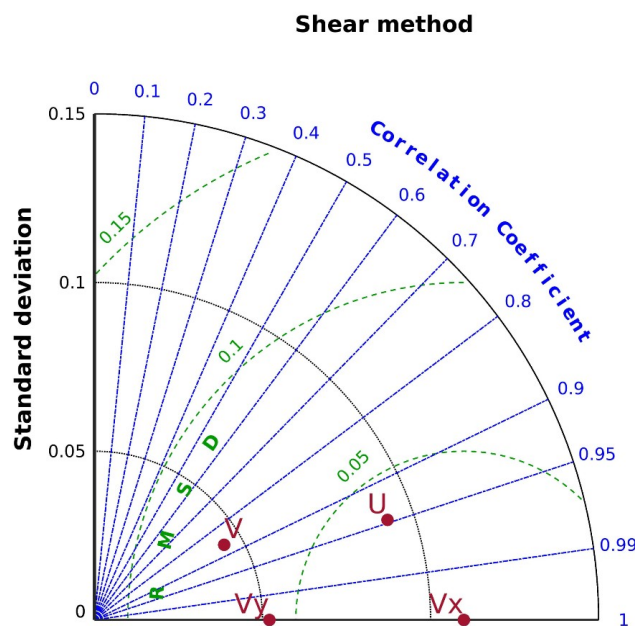
**Figure 3.14**: Taylor's diagram compares DACs (Vx, Vy), and ADCP-derived residual current (U, V)—respectively for each component of eastward and northward velocity—along the section of interest, for the "shear method".

Statistical analysis is performed with the eastward and northward components considered separately. The Taylor diagram shows a good agreement between the DAC (used as a reference) and the ADCP-derived residual currents (Fig. 3.14). The correlation coefficient for the east-west and north-south components is 0.95 and 0.88, respectively, with a *p-value* <0.001. Furthermore, the average standard deviation is between 0.04 and 0.08 m s$^{-1}$, while the average RMSD is between 0.04 and 0.06 m s$^{-1}$. These results give us some confidence in the "shear" method used to estimate absolute velocities. In this chapter, we showed the results on one glider section for the toolbox, but these ADCP and DAC velocities were compared across all deployments and will be presented in Chapter 4. Finally, the L3 matrix file containing all derived parameters is generated.

### 3.4.7. Step 6: mapping & gridding – output level 4 files

For some applications or analyses, the user may find it more convenient to use the data projected along a section, instead of as continuous measurements along the glider trajectory. In this

step, the glider data are projected from reference positions entered by the user (latitude/longitude). This allows us to estimate the distances (km) of each profile from a point of origin (the coast in our study case). Figure 3.15 shows the projection of glider data and distance from the coast estimated on the SOI. It is often more convenient, computationally efficient, and required for certain calculations to work with data that is on a regular grid. Projected glider data are interpolated on a regular 2DV grid (distance, depth) defined by the user. Once the data are projected and gridded, it is possible to estimate some spatiotemporal parameters such as currents perpendicular to the glider trajectory by the geostrophic approach (i.e., Coriolis force and impact of the horizontal density gradient). At the end of these operations, the L4 matrix file containing the final processed glider data is generated.

### 3.4.8. Step 7: plot sections

In the last step of the glider-ADCP toolbox, the processed data are plotted if the user selected it in the *Glider_ADCP_define_param.m*. A dialog box is displayed with the different physical, bio-optical, and acoustic variables to represent. Figure 3.16 shows an example with processed temperature on the SOI in spatial and temporal dimensions.
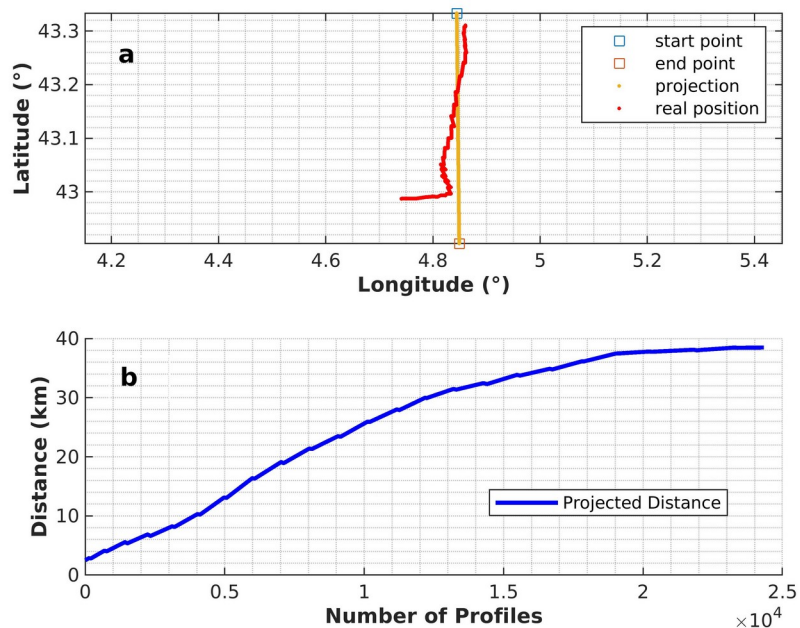
**Figure 3.15**: (a) The red line corresponds to the glider section and the orange line is the projected section from the two reference positions. (b) Distance from the coast (km) estimated along the glider projected section.
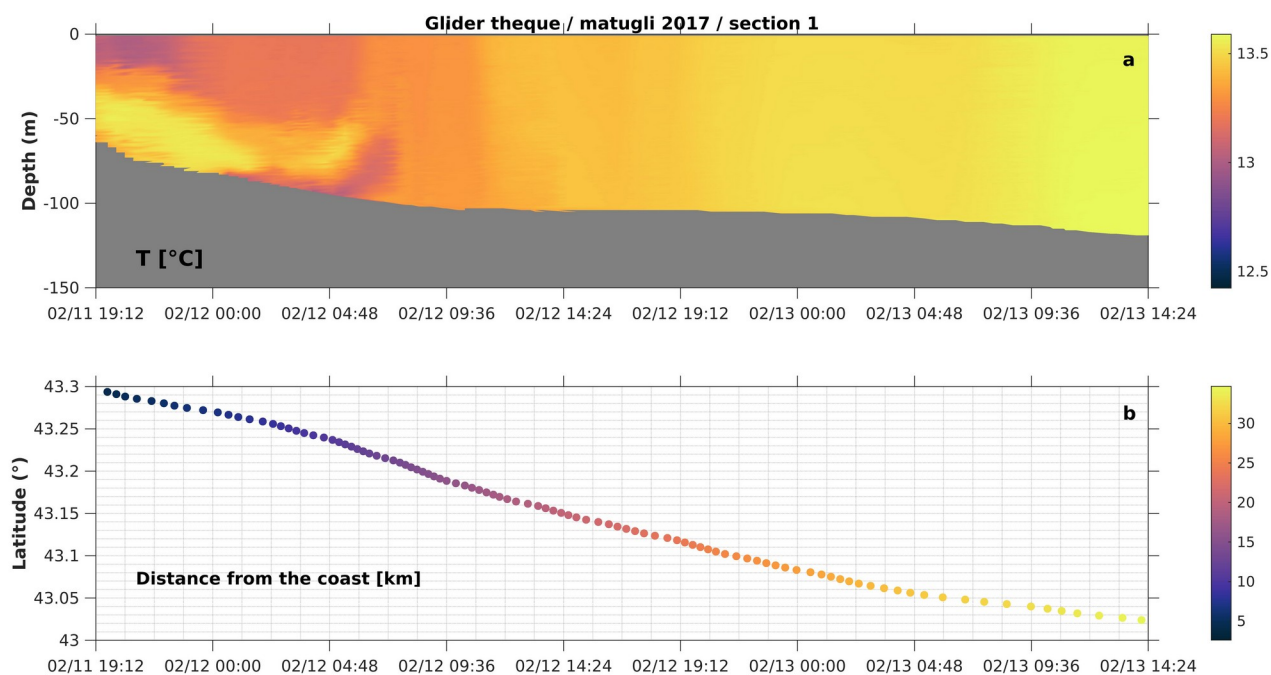


**Figure 3.16**: (a) Glider time series of temperature. (b) Glider distance from the coast (km) as a function of time.

# References

Davis, R. E., Eriksen, C. C., Jones, C. P., 2002. Autonomous buoyancy-driven underwater gliders. The technology and applications of autonomous underwater vehicles 37–58.

EGO gliders data management team, 2017. EGO Gliders NetCDF Format Reference Manual.

Eriksen, C.C., Osse, T.J., Light, R.D., Wen, T., Lehman, T.W., Sabin, P.L., Ballard, J.W., Chiodi, A.M., 2001. Seaglider: A long-range autonomous underwater vehicle for oceanographic research. IEEE Journal of oceanic Engineering 26, 424–436.

Firing, E., Gordon, R. L., 1990. Deep ocean acoustic Doppler current profiling. Presented at the Proceedings of the IEEE Fourth Working Conference on Current Measurement, IEEE, pp. 192–201.

Francois, R., Garrison, G., 1982. Sound absorption based on ocean measurements. Part II: Boric acid contribution and equation for total absorption. The Journal of the Acoustical Society of America 72, 1879–1890.

Garau, B., Ruiz, S., Zhang, W.G., Pascual, A., Heslop, E., Kerfoot, J., Tintoré, J., 2011. Thermal lag correction on Slocum CTD glider data. Journal of Atmospheric and Oceanic Technology 28, 1065–1071.

Gentil, M., Many, G., Durrieu de Madron, X., Cauchy, P., Pairaud, I., Testor, P., Verney, R., Bourrin, F., 2020. Glider-Based Active Acoustic Monitoring of Currents and Turbidity in the Coastal Zone. Remote Sensing 12, 2875.

Gordon, R. L., 1996. Acoustic Doppler current profiler-Principles of operation: A practical primer. Rd Instruments 54, 54.

Gregor, L., Ryan-Keogh, T.J., Nicholson, S.-A., Du Plessis, M., Giddy, I., Swart, S., 2019. GliderTools: A Python toolbox for processing underwater glider data. Frontiers in Marine Science 6, 738.

Liblik, T., Karstensen, J., Testor, P., Alenius, P., Hayes, D., Ruiz, S., Heywood, K., Pouliquen, S., Mortier, L., Mauri, Ejm., 2016. Potential for an underwater glider component as part of the Global Ocean Observing System. Methods in Oceanography 17, 50–82.

Margirier, F., Bosse, A., Testor, P., l'Hévéder, B., Mortier, L., Smeed, D., 2017. Characterization of convective plumes associated with oceanic deep convection in the northwestern Mediterranean from high-resolution in situ data collected by gliders. Journal of Geophysical Research: Oceans 122, 9814–9826.

MATLAB, 2018. 9.7.0.1190202 (R2019b). The MathWorks Inc., Natick, Massachusetts.

McDougall, T.J., Barker, P. M., 2011. Getting started with TEOS-10 and the Gibbs Seawater (GSW) oceanographic toolbox. SCOR/IAPSO WG 127, 1–28.

Merckelbach, L., Berger, A., Krahmann, G., Dengler, M., Carpenter, J.R., 2019. A dynamic flight model for Slocum gliders and implications for turbulence microstructure measurements. Journal of Atmospheric and Oceanic Technology 36, 281–296.

Merckelbach, L., Smeed, D., Griffiths, G., 2010. Vertical water velocities from underwater gliders. Journal of Atmospheric and Oceanic Technology 27, 547–563.

Miles, T., Slade, W., Glenn, S., 2021. Sediment resuspension and transport from a glider integrated Laser In Situ Scattering and Transmissometry (LISST) particle analyzer. Journal of Atmospheric and Oceanic Technology.

Miles, T. N., Kohut, J., Slade, W., Gong, D., 2018. Suspended particle characteristics from a glider integrated LISST sensor. Presented at the OCEANS 2018 MTS/IEEE Charleston, IEEE, pp. 1–5.

Mullison, J., 2017. Backscatter estimation using broadband acoustic doppler current profilers-updated. Presented at the Proceedings of the ASCE Hydraulic Measurements & Experimental Methods Conference, Durham, NH, USA, pp. 9–12.

Mullison, J., DeCollibus, C., Allsup, B., 2013. An investigation of the accuracy of current profile measurements from a glider-mounted ADCP operating in shallow water. Presented at the 2013 OCEANS-San Diego, IEEE, pp. 1–8.

Palmer, M.R., Stephenson, G.R., Inall, M.E., Balfour, C., Düsterhus, A., Green, J.A.M., 2015. Turbulence and mixing by internal waves in the Celtic Sea determined from ocean glider microstructure measurements. Journal of Marine Systems 144, 57–69.

Rudnick, D. L., 2016. Ocean research enabled by underwater gliders. Annual review of marine science 8, 519–541.

Rudnick, D. L., Davis, R. E., Eriksen, C. C., Fratantoni, D. M., Perry, M. J., 2004. Underwater gliders for ocean research. Marine Technology Society Journal 38, 73–84.

Rudnick, D. L., Sherman, J. T., Wu, A.P., 2018. Depth-average velocity from Spray underwater gliders. Journal of Atmospheric and Oceanic Technology 35, 1665–1673.

Teledyne Webb Research, 2012. Slocum G2 Glider Maintenance Manual.

Testor, P., de Young, B., Rudnick, D. L., Glenn, S., Hayes, D., Lee, C. M., Pattiaratchi, C., Hill, K., Heslop, E., Turpin, V., 2019. OceanGliders: a component of the integrated GOOS. Frontiers in Marine Science 6, 422.

Todd, R. E., Rudnick, D. L., Sherman, J. T., Owens, W. B., George, L., 2017. Absolute Velocity Estimates from Autonomous Underwater Gliders Equipped with Doppler Current Profilers. Journal of Atmospheric and Oceanic Technology 34, 309—333. https://doi.org/10.1175/JTECH-D-16-0156.1

Troupin, C., Beltran, J.P., Heslop, E., Torner, M., Garau, B., Allen, J., Ruiz, S., Tintoré, J., 2015. A toolbox for glider data processing and management. Methods in Oceanography 13, 13–23.

Visbeck, M., 2002. Deep velocity profiling using lowered acoustic Doppler current profilers: Bottom track and inverse solutions. Journal of atmospheric and oceanic technology 19, 794–807.

Wolk, F., Lueck, R., Laurent, L.S., 2009. Turbulence measurements from a glider. Presented at the OCEANS 2009, IEEE, pp. 1–6.